5-10-2005

Quantum cascade laser gain medium modeling using a second-nearest-neighbor sp3s* tight-binding model

Jeremy Green
University of Glasgow

Timothy B. Boykin
University of Alabama, Huntsville

Corrie D. Farmer
University of Glasgow

Michael Garcia
Thales Research and Technology

Charles N. Ironside
University of Glasgow

See next page for additional authors

ELSEVIER

Superlattices and Microstructures 37 (2005) 410–424

Superlattices and Microstructures

www.elsevier.com/locate/superlattices

Quantum cascade laser gain medium modeling using a second-nearest-neighbor sp^3s^* tight-binding model

Jeremy Green[a,*], Timothy B. Boykin[b], Corrie D. Farmer[a], Michel Garcia[c], Charles N. Ironside[a], Gerhard Klimeck[d,e], Roger Lake[f], Colin R. Stanley[a]

[a] *Department of Electronics and Electrical Engineering, University of Glasgow, Oakfield Avenue, Glasgow G12 8LT, UK*

[b] *Department of Electrical and Computer Engineering, University of Alabama in Huntsville, Huntsville, AL 35899, USA*

[c] *Thales Research and Technology, 91404 Orsay Cedex, France*

[d] *Network for Computational Nanotechnology at Purdue University, West Lafayette, IN 47907, USA*

[e] *Jet Propulsion Laboratory, California Institute of Technology, 4800 Oak Grove Drive, MS 169-315 Pasadena, CA 91109-8099, USA*

[f] *Department of Electrical Engineering, University of California, Riverside, CA 92521-0425, USA*

Received 11 February 2005; received in revised form 18 March 2005; accepted 24 March 2005
Available online 10 May 2005

Abstract

A ten-band sp^3s^* second-nearest-neighbor tight-binding model has been used to model the electronic structure of various $Al_xGa_{1-x}As$ quantum cascade laser gain media. The results of the calculations have been compared with experimental emission wavelength data, and it has been shown that the model predicts the photon energies at the peaks in the gain coefficient spectra agreeing, on average, to within 4 meV of the experimental values. Comparison of the results of the calculations with results from a two-band $\vec{k} \cdot \vec{p}$ model shows that the tight-binding model is able to find the X-like states simultaneously with the Γ-like states. These X-like states were found to be strongly localized within the barriers. Finally, the model has also been applied to InAs/AlSb and InAs/AlSb/GaSb QCLs.

* Corresponding author.
E-mail address: qcl@jeremygreen.me.uk (J. Green).

0749-6036/$ - see front matter © 2005 Elsevier Ltd. All rights reserved.
doi:10.1016/j.spmi.2005.03.003

Keywords: Quantum cascade laser; Tight-binding; Second-nearest-neighbor; Intersubband; Gas sensing; Gas detection; Antimonide

1. Introduction

The quantum cascade laser (QCL) is an electrically pumped semiconductor laser that emits in the mid-infrared region of the electromagnetic spectrum. Unlike most semiconductor injection lasers, which use electron–hole recombination to generate gain, the QCL is unipolar and light emission takes place when electrons undergo transitions between confinement-induced energy levels in just one band. The first demonstration of the successful operation of a QCL was presented in [1], and was based on a design for an electrically pumped intersubband optical amplifier [2,3].

The main application of QCLs is for gas sensing since they have been made to emit at wavelengths in the range of at least ∼3.5 μm [4] to 106 μm [5], which overlaps the region of the electromagnetic spectrum containing molecular absorption bands. Optimization of the maximum operating temperature, threshold current, output power and careful control of the emission wavelength range are required to exploit fully the capabilities of QCLs. However, the large space available for QCL gain medium design means that an accurate tool is required to select those designs that should be carried forward for expensive and time-consuming growth, fabrication, testing and, ultimately, production.

This paper presents the results of calculations performed using the NanoElectronic MOdeling 3.0.2 software package (NEMO) [6], which is a candidate for such a tool. NEMO was developed by the Applied Research Laboratory of Raytheon TI Systems and others as a comprehensive quantum device modeling package, and is based on the non-equilibrium Green's function formalism. Previously, NEMO has been used for the modeling of resonant tunneling diodes [7–9]. Here, one of its sp^3s^* tight-binding models has been used to make predictions of the photon energies, E_{peak}, at which the gain coefficients of several three-well GaAs/$Al_xGa_{1-x}As$ QCL gain media are maximized. These predictions are compared to experimental results, before the first tight-binding calculations of the electronic structure of Sb-based QCLs are made.

With a few caveats [10,11], sp^3s^* tight-binding models [12] offer the possibility of modeling the electronic structure of a III–V heterostructure where transport can take place via any valley. They are also able to model accurately the conduction band nonparabolicity for Γ-like states. Both of these capabilities are potentially important in a QCL, where quantum confinement pushes the resonant states far above the bulk conduction band edge of the well material. The atomic-like basis states used in a tight-binding model should be better suited to modeling the electronic structure of a QCL than the bulk basis states used in a $\vec{k} \cdot \vec{p}$ model. The latter set of states should be reserved for modeling heterostructures with layer thicknesses much greater than a monolayer, where the bulk electronic structures are only weakly perturbed.

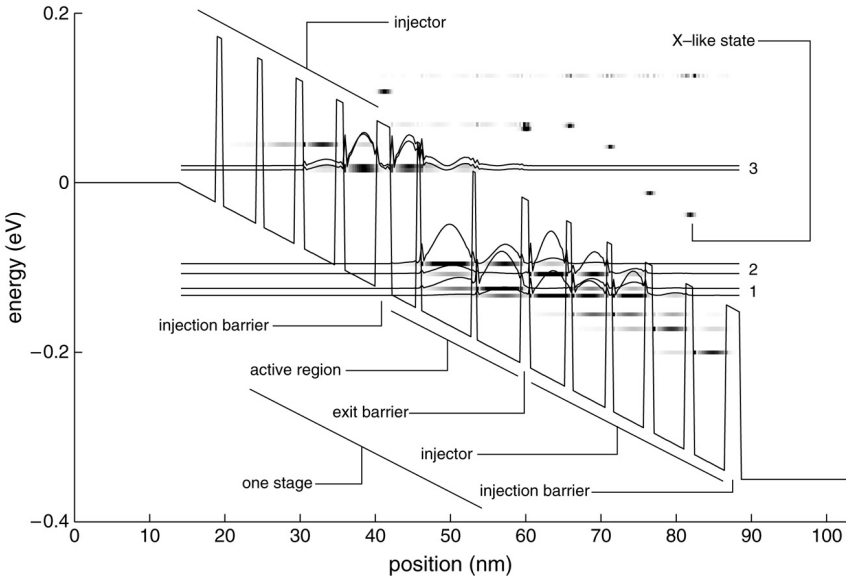

Fig. 1. Resonant states found for the AlAs/GaAs design of Becker et al. [13] using a second-nearest-neighbor sp^3s^* tight-binding model. The moduli squared of the sums of the tight-binding expansion coefficients are shown for each lattice plane. They are represented for all the resonant states using gray-scale bars and, in addition, for the labeled pairs of states forming levels 1, 2 and 3, with curves. The electric field minimizes the splitting of the two states forming level 3. The bulk conduction band edge energy is also plotted: for the AlAs barriers, this is the bulk X-valley energy.

2. Nomenclature

Before discussing the calculations, it is necessary to clarify the nomenclature used to describe the electronic resonant states in a QCL. The terms level 1, level 2 and level 3 are often used to describe the lowest, second-lowest and third-lowest energy resonant states in a biased three-well active region sandwiched not between the injector superlattices of a periodically repeated structure, but barriers that are thick compared with the wave function decay lengths. (The terminology used to describe the various layers in a three-well QCL gain medium is indicated in Fig. 1.) The introduction of the proper injection and exit barriers and the injector superlattices on both sides of the active region introduces extra states mostly localized in the injectors, but with some overlap with the active region states. As the electric field applied to the device is altered, these states anti-cross with the states in the active region, causing them to split. The most useful labeling scheme in this more realistic picture, and the one used in this work (see Fig. 1), is to assign the terms level 1, 2 and 3 to the anti-crossed *pairs* of states in each active region.

Mid-infrared gain is produced by setting up a population inversion between levels 2 and 3 by engineering the device structure to maximize the non-radiative lifetime of level 3, the stimulated emission rate from level 3 to level 2 and the polar optical phonon scattering rate from level 2 to level 1.

3. Method

3.1. Choice of calculation domain

A QCL gain medium contains typically 25–35 repeated stages, each comprising an injector, an injection barrier, an active region and an exit barrier. It is not feasible or useful to model such a large structure directly. Instead, the electronic structure of a single period from an infinitely repeated set of QCL stages was approximated using a biased injector superlattice/injection barrier/active region/exit barrier/injector superlattice/injection barrier structure, i.e. about one and a half stages. This structure was chosen to model accurately the energies and tight-binding model expansion coefficients of the six states (three pairs) labeled 1, 2 and 3 in Fig. 1. Note that, for states localized close to the edge of the domain (for example, the lowest-energy state shown in Fig. 1), the states will only approximate poorly to those in an infinite set of stages. This domain was chosen since, for the structures investigated, level 3 of the active region is split by an interaction with a state mostly localized in just the last two wells of the preceding injector. It is therefore not necessary to include an injection barrier on the upstream side. An injection barrier is required on the downstream side of the domain since the states in the right-hand injector superlattice that split levels 1 and 2 generally have a significant penetration into the downstream injection barrier. For the unperturbed A1737 design mentioned in Section 4.2, the effect of varying the number of layers included in the calculation domain was investigated, and the above choice found to predict the real parts of the eigenenergies satisfactorily.

3.2. Electronic structure model

A second-nearest-neighbor tight-binding model [10] with spin–orbit coupling and explicit inclusion of up and down spin states was used to model the electronic structure of the lasers. For GaAs and AlAs, model parameters were taken from [10]. The conduction band offset between GaAs and AlAs was taken to be 1.05244 eV. For $Al_{0.3}Ga_{0.7}As$, a conduction band offset of 0.22661 eV with respect to GaAs and the parameters given in Table 1 were used. These parameters, which have not been published previously, were manually optimized to fit various characteristics of the bulk band structure to room-temperature experimental values. The manual optimization was greatly simplified by using the analytic band-edge energy and effective-mass formulae presented in [10]. It is worth drawing attention here to the automatic method presented in [11] for optimizing such parameters, which would greatly reduce the work involved in finding further sets. For other Al contents, tight-binding parameter sets and conduction band offsets were linearly interpolated between the values for GaAs, $Al_{0.3}Ga_{0.7}As$ and AlAs. A monolayer thickness of 0.2833 nm was used for all Al contents.

The charge on the free carriers and ionized dopant ions in a QCL will affect the energies and wave functions of the resonant states. For these calculations, these effects have been ignored and the electrostatic potential has been assumed to drop linearly across the active region. No scattering self-energies were used and the electronic states were all found for zero in-plane momentum.

Table 1
Second-nearest-neighbor sp^3s^* tight-binding model parameters (given in eV) for $Al_{0.3}Ga_{0.7}As$ using the notation of [10], which is based on that of [14]

$E^{(000)}_{sa,sa}$	−8.204 079	$4E^{(110)}_{s^*a,xa}$	0.020 000
$E^{(000)}_{pa,pa}$	0.366 741	$4E^{(011)}_{s^*a,xa}$	0.058 000
$E^{(000)}_{s^*a,s^*a}$	8.093 021	$4E^{(110)}_{xa,xa}$	0.404 660
$E^{(000)}_{sc,sc}$	−2.549 169	$4E^{(011)}_{xa,xa}$	−0.221 180
$E^{(000)}_{pc,pc}$	3.331 271	$4E^{(110)}_{xa,ya}$	1.066 000
$E^{(000)}_{s^*c,s^*c}$	6.341 051	$4E^{(011)}_{xa,ya}$	−1.060 000
$4E^{(\frac{1}{2}\frac{1}{2}\frac{1}{2})}_{sa,sc}$	−6.640 000	$4E^{(110)}_{sc,sc}$	−0.017 000
$4E^{(\frac{1}{2}\frac{1}{2}\frac{1}{2})}_{sa,pc}$	4.900 000	$4E^{(110)}_{sc,xc}$	0.072 300
$4E^{(\frac{1}{2}\frac{1}{2}\frac{1}{2})}_{s^*a,pc}$	4.239 000	$4E^{(011)}_{sc,xc}$	0.026 000
$4E^{(\frac{1}{2}\frac{1}{2}\frac{1}{2})}_{pa,sc}$	8.230 000	$4E^{(110)}_{s^*c,xc}$	0.016 000
$4E^{(\frac{1}{2}\frac{1}{2}\frac{1}{2})}_{pa,s^*c}$	4.725 000	$4E^{(011)}_{s^*c,xc}$	0.074 450
$4E^{(\frac{1}{2}\frac{1}{2}\frac{1}{2})}_{x,x}$	2.077 870	$4E^{(110)}_{xc,xc}$	0.344 600
$4E^{(\frac{1}{2}\frac{1}{2}\frac{1}{2})}_{x,y}$	5.074 000	$4E^{(011)}_{xc,xc}$	−0.120 080
$4E^{(110)}_{sa,sa}$	−0.010 000	$4E^{(110)}_{xc,yc}$	0.681 000
$4E^{(110)}_{sa,xa}$	0.047 000	$4E^{(011)}_{xc,yc}$	−1.420 000
$4E^{(011)}_{sa,xa}$	0.052 600	λ_a	0.140 000
		λ_c	0.043 000

The $4E^{(110)}_{s^*a,s^*a}$, $4E^{(110)}_{s^*c,s^*c}$, $4E^{(110)}_{sa,s^*a}$ and $4E^{(110)}_{sc,s^*c}$ parameters were all set to zero.

3.3. Threshold electric field determination

The separations in energy of the states forming levels 2 and 3 depend on the externally applied electric field. To find the field at laser threshold rigorously, it would be necessary to evaluate the gain coefficient and current density as a function of electric field, before finding the field that sets the round-trip modal gain equal to the round-trip loss for a particular waveguide design. For this work, these calculations were not performed, and instead, two simplified procedures were used to set the electric field. The first procedure involved finding the voltage drop across each structure (to the nearest 0.01 V) that minimized the splitting in energy of level 3. This procedure maximizes the rate at which electrons can tunnel through the injection barrier [2], ensuring that this is not the rate-limiting step for electronic transport. The second procedure minimized the splitting of level 1. There is evidence that tunneling through the exit barrier constitutes a bottleneck

Table 2
The designs that were modeled, the references the experimental results were taken from and the temperatures at which the measurements were made

Gain medium design	Experimental data	Temperature (K)
Kruck et al. [16]	[16]	250
Sirtori et al. [17]	[17]	77
A1516 [this paper]	[This paper]	236
A1586 [this paper]	[This paper]	237
Becker et al. [13]	[13]	77

for electronic transport in three-quantum-well QCLs [15], so this procedure may be more realistic physically.

3.4. Modeled designs

To assess the predictions made by the sp^3s^* model, the designs given in Table 2 were modeled and predictions of the photon energy, E_{peak}, that maximizes the gain coefficient were compared to experimental results. Wafers A1516 and A1586 (see [18] and [19] respectively) were designed and grown at Glasgow University and are based on the design of Kruck et al. [16]. A stage from the gain medium in wafer A1516 has layer thicknesses of **51** / 19 / ***11*** / 56 / **11** / 49 / **28** / 36 / **17** / 32 / **20** / 28 / **22** / 27 / **26** / 27 Å. For A1586, the thicknesses are **51** / 19 / ***11*** / 60 / **11** / 49 / **28** / 36 / **17** / 32 / **20** / 28 / **22** / 27 / **26** / 27 Å. For both designs, bold type indicates $Al_{0.33}Ga_{0.77}As$ layers; bold italic type indicates $Al_{0.4}Ga_{0.6}As$; normal type indicates GaAs and the underlined layers are doped with Si to give a sheet doping density of 8.23×10^{12} cm^{-2} per stage.

3.5. Experimental data for comparison

For the design of Kruck et al. [16], the experimental E_{peak} was taken from the plot of the electroluminescence spectrum in figure 2 of [16]. For the design of Sirtori et al. [17], the value was taken from the text of [17], which gives the wavelength for single-mode lasing for a Fabry–Perot (FP) device. Their device only lased up to 140 K, and they only quoted an emission wavelength at 77 K, so this value is used here in place of a value for 300 K. The peaks in the gain coefficient for A1516, A1586 and the design of Becker et al. [13] were assumed to be at the same photon energies as the peaks of the envelopes of the multi-mode emission intensity spectra of FP lasers. For A1516, a spectrum was measured for a wet-etched 20 μm by 1.5 mm FP device using a Bomem DA-3 Fourier-transform spectrometer. For A1586, the measurements were made with a Fourier-transform spectrometer at Rutherford–Appleton Laboratories on a facet-coated 21.4 μm by 0.9 mm FP device [19]. The value for the design of Becker et al. was taken from the caption of figure 2 of [13]. The results in [20] suggest that E_{peak} will decrease by about 4% as the temperature of the active region is changed from 77 to 300 K, so the lack of near-room-temperature data for some of the designs should not change the qualitative conclusions of this paper.

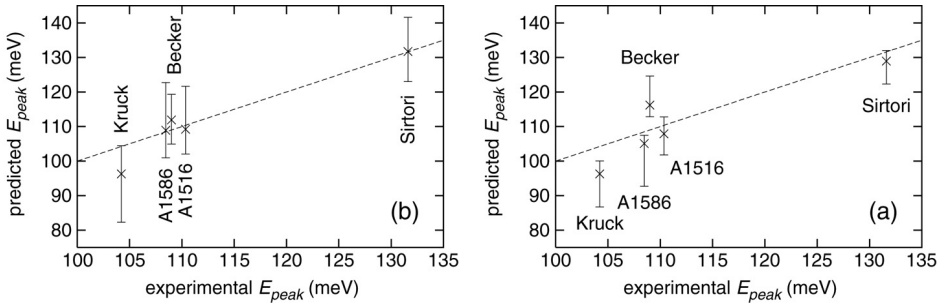

Fig. 2. Comparison of experimental results with modeling for the designs listed in Table 2. E_{peak} is the photon energy that maximizes the gain coefficient and the straight lines show the ideal case of perfect agreement between the experimental results and the modeling. The methods used to predict the bounds on E_{peak} are described in the body of the paper, while the crosses show the predictions made using expression (1). The voltage drop is set to minimize the level 3 splitting in (a) and the level 1 splitting in (b).

4. Results and discussion

4.1. Emission wavelength predictions

The electronic structure found for the gain medium design of Becker et al. is shown in Fig. 1 for an electric field that minimizes the splitting of level 3. Explicit calculation of the gain coefficient from the resonant state energies and the tight-binding model expansion coefficients was not implemented for this work, so, initially, bounds on the photon energy, E_{peak}, that maximizes the gain coefficient were estimated from just the energies of the states. Different methods were used to find the bounds depending on whether the voltage drop across the modeled region was set to minimize the splitting of level 1 or level 3. If the energies of the two states forming level i are $E_{i,1}$ and $E_{i,2}$, where $E_{i,1} < E_{i,2}$, then, for the voltage drop that minimizes the splitting of level 3, the upper bound on E_{peak} was taken as $(E_{3,1} + E_{3,2})/2 - E_{2,1}$ and the lower bound as $(E_{3,1} + E_{3,2})/2 - E_{2,2}$. This procedure was used since, in a properly designed QCL, the splitting of level 3 is chosen so that the broadening of the levels merges the local density of states of the pair of states into a single peak [21]. For the voltage drop that minimizes the splitting of level 1, the lower bound was taken as $E_{3,1} - E_{2,2}$ and the upper bound as $E_{3,2} - E_{2,1}$.

These bounds are compared with the experimental results in Fig. 2. The results show that, for the gain media considered, the two models predict E_{peak} to within at worst 21% of the experimental value. The results do not show that one method for choosing the electric field is any better than the other. These bounds are relatively wide, and do not do justice to the accuracy of the electronic structure calculations. Ideally, a rate equation model for the gain coefficient should be adopted, but NEMO is currently unable to calculate intersubband scattering rates with its multi-band models. Instead, estimates for E_{peak} were made by using the overlaps of the probability densities of the states forming levels 2 and 3 to form a weighted average of the four possible level 3–level 2 energy differences:

$$E_{\text{peak}} \approx \frac{\sum_{i\in\{1,2\}} \sum_{j\in\{1,2\}} \text{Re}(E_{3,j} - E_{2,i})\, f_{i,j}}{\sum_{i\in\{1,2\}} \sum_{j\in\{1,2\}} f_{i,j}} \tag{1}$$

where:

$$f_{i,j} = \sum_{\text{device region}} |\psi(E_{2,i})|^2 |\psi(E_{3,j})|^2 \tag{2}$$

$$\psi(E) = \sum_n c_n(E) \tag{3}$$

$$c_n = \text{expansion coefficient for } n\text{th orbital.} \tag{4}$$

Fig. 2 shows that the agreement between the predictions made using this empirical model and experiment is good, especially for the electric field that minimizes the splitting of level 1. The root-mean-square discrepancy with experiment is 5 meV for the electric field that minimizes the level 3 splitting, and 4 meV for the electric field minimizing the level 1 splitting. The latter result is dominated by the relatively large discrepancy for the design of Kruck et al. [16]: without this value, the RMS discrepancy is 1.58 meV.

4.2. Layer thickness rounding

Since NEMO uses an atomistic tight-binding model, all layer thicknesses must be specified as a whole number of monolayers (MLs). The layer thicknesses for the structures listed in Table 2 are not multiples of the GaAs ML spacing in general, and so had to be rounded before being included in the calculations. To investigate the extent to which this rounding might affect the results, three calculations were performed where the layer thicknesses of a gain medium (A1737 [22]) were (1) left unchanged, (2) increased by one ML and (3) decreased by one ML. Gain medium A1737 is based on A1586, and has the following layer thicknesses: **16** / 6 / ***4*** / 21 / **4** / 16 / **10** / 13 / **6** / 11 / **7** / 10 / **8** / 10 / **9** / 10 ML. The same notation as used in Section 3 to describe the compositions and doping of A1516 and A1586 has been used here. The sheet doping density per stage was 7.91×10^{12} cm^{-2}. The bounds on E_{peak} for these calculations are presented in Fig. 3 and were found by the same procedure as used to find the bounds in Fig. 2(a). Also shown are predictions made using expression (1). To model this effect properly, the model should also take into account interface roughness. However, these results show that, for this design at least, it is more important to include the injector-induced splittings of levels 2 and 3 in a model that aims to predict E_{peak} than correlated thickness variations of ± 1 ML.

4.3. Comparison with empirical two-band $\vec{k} \cdot \vec{p}$ model

The two-band empirical $\vec{k} \cdot \vec{p}$ model [23,24] is used by many groups to predict the state separations in QCLs with reasonable accuracy: for example, for the design of Becker et al., this model has been used [13] to predict a value of 109 meV for E_{peak}, which, to three significant figures, was identical to the experimental value at 77 K. The main advantage that the sp^3s^* model presented here has over the two-band empirical $\vec{k} \cdot \vec{p}$ model is its ability to model the X-like states directly. These states, which are all localized within the barriers, are present in Fig. 1, but are absent in Fig. 4, where the calculation for the design

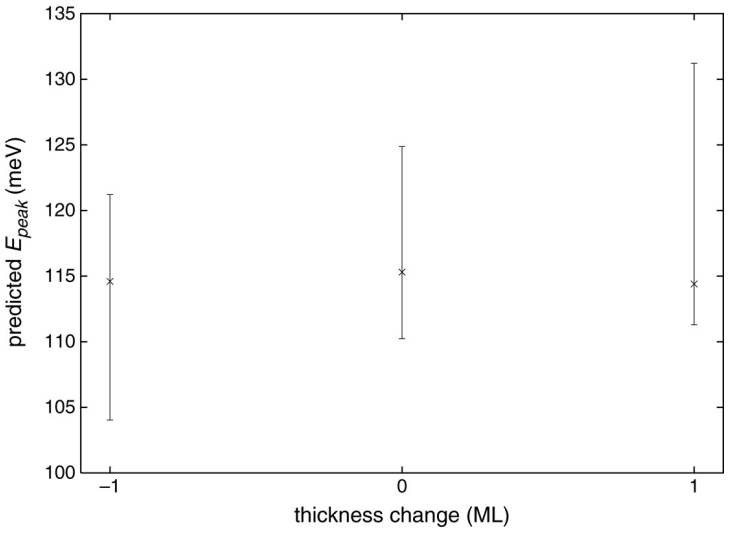

Fig. 3. Predicted bounds on photon energies, E_{peak}, that maximize the gain coefficient for gain medium A1737 and structures formed by increasing/decreasing all layer thickness by one monolayer (ML). The voltage drop across the modeled region was chosen to minimize the separation of the pair of states forming level 3. The crosses show the values of E_{peak} predicted using expression (1).

of Becker et al. was repeated using NEMO's two-band $\vec{k} \cdot \vec{p}$ model. (It can also be seen that there are some above-barrier resonances in Fig. 4 that are not present in Fig. 1. This is an artifact of the numerical method used to resolve the resonant states.)

Table 3 shows the resonant state energies for the electronic structures presented in Figs. 1 and 4. While the level splittings, to the nearest meV, predicted by the two models are almost identical, an estimate for E_{peak} found using expression (1) and the two-band $\vec{k} \cdot \vec{p}$ model results gives an energy of 127 meV. Examination of Fig. 2(a) shows that this prediction is significantly less accurate than the predictions made using the second-nearest-neighbor sp^3s^* tight-binding model.

Empirically tuning the two-band model's parameters to model better the electronic structure further in energy from the bulk band edge could improve this prediction. However, the empirical two-band model only has $n + 1$ adjustable parameters for an n material heterostructure: for example, for a single material, the bulk imaginary dispersion relation cannot be set independently of the effective mass and nonparabolicity parameters and for two materials, the nonparabolicity parameter can only be set for one of the materials. The sp^3s^* tight-binding model used in this work has 37 parameters per material, providing for better modeling of the detailed alignment between the resonant states in each active region and its neighboring injector superlattices.

4.4. Antimonide system

The InAs/AlSb/GaSb material system offers a Γ-point conduction band offset of over 2 eV, and is therefore an interesting candidate for the production of short-wavelength

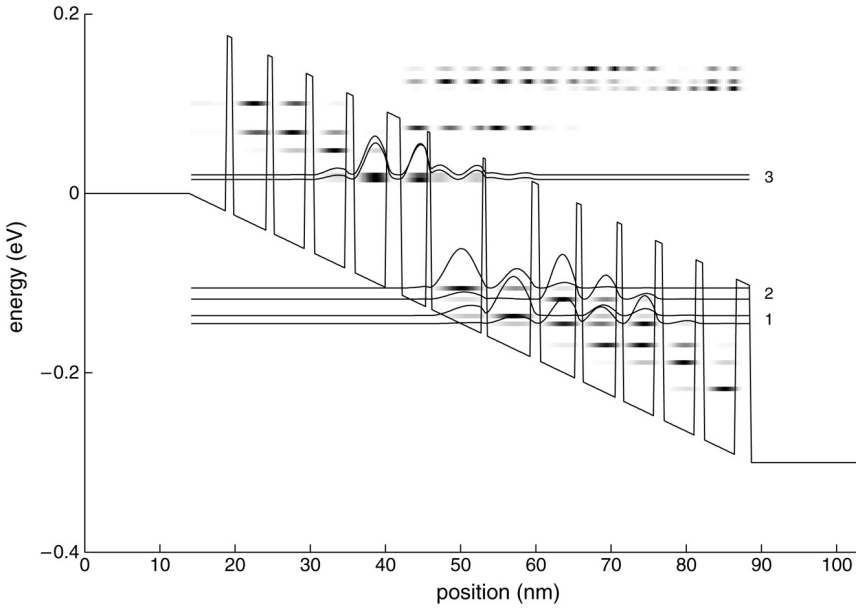

Fig. 4. Resonant states found for the AlAs/GaAs design of Becker et al. [13] using a two-band $\vec{k} \cdot \vec{p}$ model. The electric field minimizes the splitting of the states forming level 3. The bulk conduction band edge energy is also plotted: for the AlAs barriers, this is the bulk X-valley energy.

Table 3
The real parts of the resonant state energies (in meV) for the electronic structures shown in Figs. 1 and 4 for the design of Becker et al. [13] (found, respectively, using second-nearest-neighbor sp^3s^* and two-band $\vec{k} \cdot \vec{p}$ models)

Level	sp^3s^*	$\vec{k} \cdot \vec{p}$
3	19.9	20.6
	14.9	15.6
2	−95.3	−105.5
	−107.1	−117.9
1	−124.6	−136.2
	−132.9	−145.0

QCLs. NEMO provides parameters sets for this material system for the second-nearest-neighbor sp^3s^* tight-binding model with spin–orbit coupling and explicit spin states described in Section 3.2. The model includes the marked nonparabolicity of the InAs Γ-valley and the indirect band-gap in the AlSb barriers, as is evident in the band structures plotted in Fig. 5, and should provide useful insights into the operation of such devices. The parameters sets have been published by Boykin [10], although for GaSb, the $4E_{xa,ya}^{(110)}$ and $4E_{xc,yc}^{(110)}$ parameters were taken as 0.569 and 0.445 eV respectively in this paper.

Ohtani et al. have published two designs for Sb-based QCLs. The electronic structure for the earlier, shorter-wavelength design [25] is shown in Fig. 6(a). This design did not

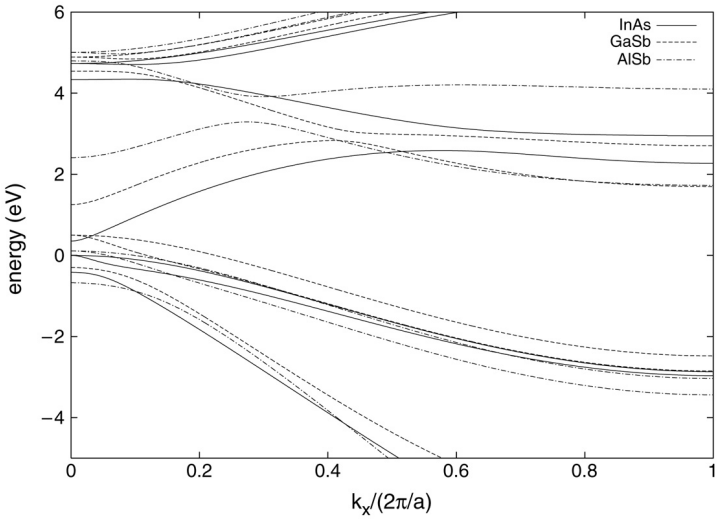

Fig. 5. Band structures for InAs, GaSb and AlSb on an InAs substrate along the ΓX line in $\vec{k}$-space, calculated by NEMO using a second-nearest-neighbor sp^3s^* tight-binding model with spin–orbit coupling and explicit inclusion of up and down spin states.

result in a functioning laser, with Ohtani et al. concluding that the narrow band-gap in the InAs system, together with the high electric field, were resulting in Zener breakdown. The electronic structure for the later, successful, longer wavelength design [26] is shown in Fig. 6(b).

Ohtani et al. present experimental data on the gain spectra for the two designs in references [25] and [26], the peak gain photon energies being 227 and 123 meV respectively. The corresponding values predicted by NEMO, which are indicated in the caption of Fig. 6, are both, to two significant figures, 17% lower then these experimental values. This suggests that the parameters used for this system might need further optimization [22] or that the structures modeled did not exactly match the structures that were grown.

5. Conclusion

NEMO has been shown to be capable of predicting the photon energy, E_{peak}, at the peak in the gain coefficient spectrum of various $Al_xGa_{1-x}As$ quantum cascade laser gain media to within, on average, 4 meV of the experimental values. The sp^3s^* tight-binding model used by NEMO is not only capable of predicting the resonant state separations, but can also directly model the X-like states. It has been shown that correlated errors in the layer thicknesses of ± 1 ML and the procedure used to set the electric field across the device are less important when determining E_{peak} than the injector-induced splittings of levels 2 and 3. Finally, NEMO has also been shown to be capable of modeling the electronic structure of InAs/AlSb and InAs/AlSb/GaSb QCLs.

The models presented in Section 4.1 do not give predictions for the gain coefficient, so, to carry this work forward, and use an sp^3s^* model to produce optimized QCL gain media,

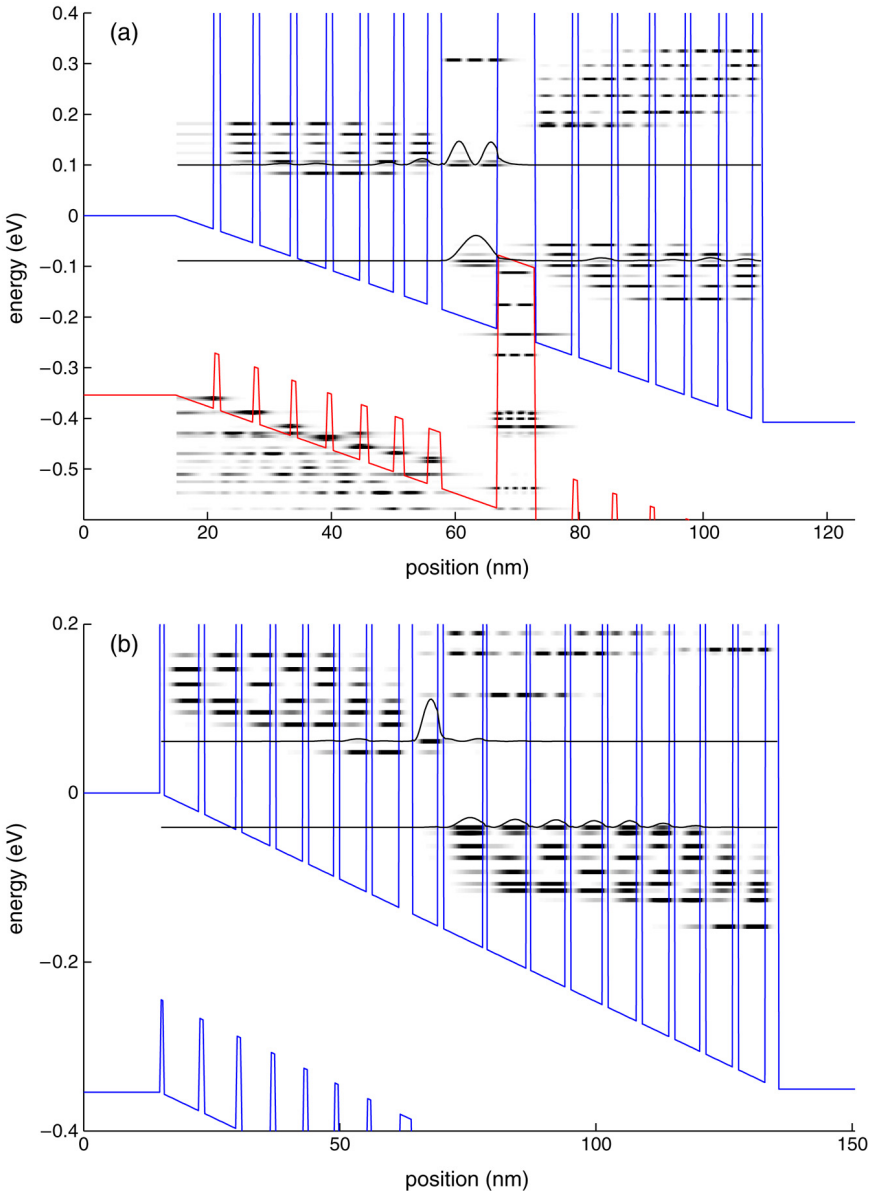

Fig. 6. Electronic structure for (a) the short-wavelength InAs/AlSb/GaSb design given in figure 1 of Ohtani et al. [25] and (b) the long-wavelength InAs/AlSb design given in figure 1 of Ohtani et al. [26]. The calculations are made using a second-nearest-neighbor sp^3s^* tight-binding model model at an electric field of (a) 43 kV cm^{-1} and (b) 29 kV cm^{-1}. The separations in energy between the two states marked with curves are (a) 189 meV and (b) 102 meV. Both the conduction band and valence band edge energies are plotted, although for (b) only the conduction band resonant states are plotted. The barrier materials are AlSb in all cases, except for one layer per stage in (a), where GaSb is used.

it will be necessary to find this quantity. This could be done using either a rate equation approach [27] or, if it can be shown to be compatible with multi-band tight-binding models, the elegant Wannier function, non-equilibrium Green's function and periodic boundary condition approach implemented by Lee and Wacker [28]. The calculation would need to take into account the injector-induced splitting of the levels, to predict single values for E_{peak} and the associated gain coefficient. The NEMO software would have to be modified so that it can calculate the polar optical phonon (POP) and optical stimulated emission scattering rates between resonant states found using its ten-band sp^3s^* models. Ideally, the electron–POP scattering rates should be found using the dielectric continuum model for phonons in a heterostructure, since modeling the scattering of electrons in QCLs using bulk phonons has been found to be inadequate [29]. Advantage should also be taken of NEMO's abilities to model properly the electronic structure of states with X-like character [30] and to model InP-system QCLs [22]. Self-consistent inclusion of quantum mechanical charge via the Hartree approximation would be a useful feature to add [22,28], as would the ability to include strained layers [4], interface roughness [28] and carrier–carrier scattering rates [31,28].

Further systematic errors in the model might include: the nonparabolicity-induced wavelength shift resulting from the neglect of the excitation of charge carriers to finite in-plane momenta at finite temperature [20] and the choice of the tight-binding model's Hamiltonian matrix elements.

Acknowledgments

Thanks are due to John R. Barker at the University of Glasgow for establishing contact with the NEMO team at JPL and UC Riverside. Thanks must also go to Fabiano Oyafuso at JPL and John H. Davies at the University of Glasgow for discussions related to this work and to Erwan Normand at Strathclyde University for performing spectral measurements on devices fabricated from wafers A1516 and A1586. This NEMO-related work serves the on-going JPL efforts on the development of far-infrared sensors and lasers. The NanoElectronic MOdeling Tool (NEMO) remains restricted to use within the United States due to export regulations. JPL has access to NEMO through a government development license, and is currently pursuing the application of NEMO to various quantum device designs as proof of concept experiments. This work was supported, in part, by the Engineering and Physical Sciences Research Council, UK and, in part, by the National Science Foundation under Grant No. EEC-0228390. The work was carried out, in part, at the Jet Propulsion Laboratory, California Institute of Technology under a contract with the National Aeronautics and Space Administration.

References

[1] J. Faist, F. Capasso, D.L. Sivco, C. Sirtori, A.L. Hutchinson, A.Y. Cho, Quantum cascade laser, Science 264 (1994) 553–556.
[2] R.F. Kazarinov, R.A. Suris, Possibility of the amplification of electromagnetic waves in a semiconductor with a superlattice, Sov. Phys. Semicond. 5 (1971) 707–709.
[3] R.F. Kazarinov, R.A. Suris, Electric and electromagnetic properties of semiconductors with a superlattice, Sov. Phys. Semicond. 6 (1972) 120–131.

[4] J. Faist, F. Capasso, D.L. Sivco, A.L. Hutchinson, S.-N.G. Chu, A.Y. Cho, Short wavelength ($\lambda \sim 3.4$ μm) quantum cascade laser based on strained (*sic*) compensated InGaAs/AlInAs, Appl. Phys. Lett. 72 (1998) 680–682.
[5] R. Köhler, A. Tredicucci, F. Beltram, H.E. Beere, E.H. Linfield, D.A. Ritchie, A.G. Davies, Quantum cascade lasers emitting at lambda greater than 100 μm, Electron. Lett. 39 (2003) 1254–1255.
[6] NEMO home page, http://dynamo.ecn.purdue.edu/~gekco/nemo/.
[7] G. Klimeck, R. Lake, R.C. Bowen, W.R. Frensley, T.S. Moisea, Quantum device simulation with a generalized tunneling formula, Appl. Phys. Lett. 67 (1995) 2539–2541.
[8] R. Lake, G. Klimeck, R.C. Bowen, D. Jovanovic, Single and multiband modeling of quantum electron transport through layered semiconductor devices, Appl. Phys. Lett. 81 (1997) 7845–7869.
[9] G. Klimeck, Indirect bandgap-like current flow in direct bandgap electron resonant tunneling diodes, Phys. Status Solidi b 226 (2001) 9–19.
[10] T.B. Boykin, Improved fits of the effective masses at Γ in the spin–orbit, second-nearest-neighbor sp^3s^* model: Results from analytic expressions, Phys. Rev. B. 56 (1997) 9613–9618.
[11] G. Klimeck, R.C. Bowen, T.B. Boykin, C. Salazar-Lazaro, T.A. Cwik, A. Stoica, Si tight-binding parameters from genetic algorithm fitting, Superlatt. Microstruct. 27 (2000) 77–88.
[12] P. Vogl, H.P. Hjalmarson, J.D. Dow, A semi-empirical tight-binding theory of the electronic structure of semiconductors, J. Phys. Chem. Solids 44 (1983) 365–378.
[13] C. Becker, C. Sirtori, H. Page, G. Glastre, V. Ortiz, X. Marcadet, M. Stellmacher, J. Nagle, AlAs/GaAs quantum cascade lasers based on large direct conduction band discontinuity, Appl. Phys. Lett. 77 (2000) 463–465.
[14] J.C. Slater, G.F. Koster, Simplified LCAO method for the periodic potential problem, Phys. Rev. 94 (1954) 1498–1524.
[15] J. Faist, D. Hofstetter, M. Beck, T. Aellen, M. Rochat, S. Blaser, Bound-to-continuum and two-phonon resonance quantum-cascade lasers for high duty cycle, high-temperature operation, IEEE J. Quant. Electron. 38 (2002) 533–546.
[16] P. Kruck, H. Page, C. Sirtori, S. Barbieri, M. Stellmacher, J. Nagle, Improved temperature performance of $Al_{0.33}Ga_{0.67}As$/GaAs quantum-cascade lasers with emission wavelength at $\lambda \approx 11$ μm, Appl. Phys. Lett. 76 (2000) 3340–3342.
[17] C. Sirtori, P. Kruck, S. Barbieri, P. Collot, J. Nagle, M. Beck, J. Faist, U. Oesterle, GaAs/AlGaAs quantum cascade lasers, Appl. Phys. Lett. 73 (1998) 3486–3488.
[18] M. Garcia, C. Farmer, C.N. Ironside, C. Stanley, GaAs-AlGaAs quantum cascade laser at $\lambda \approx 10.5$ μm working above zero degree Celsius, Quant. Electron. Photonics 15 (2001) (poster P2-3).
[19] C.D. Farmer, C.R. Stanley, C.N. Ironside, M. Garcia, Improved GaAs-based quantum cascade laser ($\lambda \sim 11$ μm) using a high-reflectivity metal facet coating, Electron. Lett. 38 (2002) 1443–1444.
[20] Y.B. Li, J.W. Cockburn, M.S. Skolnick, J.P. Duck, M.J. Birkett, I.A. Larkin, R. Grey, G. Hill, M. Hopkinson, Mid-infrared intersubband electroluminescence from a single-period GaAs/AlGaAs triple barrier structure, Appl. Phys. Lett. 72 (1998) 2141–2143.
[21] C. Sirtori, F. Capasso, J. Faist, A.L. Hutchinson, D.L. Sivco, A.Y. Cho, Resonant tunneling in quantum cascade lasers, IEEE J. Quant. Electron. 34 (1998) 1722–1729.
[22] J. Green, Design and fabrication of quantum cascade lasers for gas sensing, Ph.D. Thesis, University of Glasgow, September 2003.
[23] D.F. Nelson, R.C. Miller, D.A. Kleinman, Band nonparabolicity effects in semiconductor quantum wells, Phys. Rev. B. 35 (1987) 7770–7773.
[24] S. White, L.J. Sham, Electronic properties of flat-band semiconductor heterostructures, Phys. Rev. Lett. 47 (1981) 879–882.
[25] K. Ohtani, H. Sakuma, H. Ohno, InAs-based quantum cascade light emitting structures containing a double plasmon waveguide, J. Cryst. Growth 241 (2003) 718–722.
[26] K. Ohtani, H. Ohno, An InAs-based intersubband quantum cascade laser, Japan. J. Appl. Phys. 41 (2002) L1279–L1280.
[27] D. Indjin, P. Harrison, R.W. Kelsall, Z. Ikonić, Self-consistent scattering theory of transport and output characteristics of quantum cascade lasers, J. Appl. Phys. 91 (2002) 9019–9026.
[28] S.-C. Lee, A. Wacker, Nonequilibrium Green's function theory for transport and gain properties of quantum cascade structures, Phys. Rev. B 66 (2002) 245314.

[29] C. Sirtori, H. Page, C. Becker, V. Ortiz, GaAs–AlGaAs quantum cascade lasers: Physics, technology, and prospects, IEEE J. Quant. Electron. 38 (2002) 547–558.
[30] L.R. Wilson, D.A. Carder, J.W. Cockburn, R.P. Green, D.G. Revin, M.J. Steer, M. Hopkinson, G. Hill, R. Airey, Intervalley scattering in GaAs/AlAs quantum cascade lasers, Appl. Phys. Lett. 81 (2002) 1378–1380.
[31] M. Rochat, L. Ajili, H. Willenberg, J. Faist, H. Beere, G. Davies, E. Linfield, D. Ritchie, Low-threshold terahertz quantum-cascade lasers, Appl. Phys. Lett. 81 (2002) 1381–1383.